

Chapter 2

Experimental Setup

In this thesis, the interaction of large xenon clusters with high intense XUV pulses has been studied in a combined scattering and spectroscopy approach. The data have been obtained at the free-electron laser in Hamburg FLASH. This chapter will give a survey on the experimental basics. In Sect. 2.1, the principles of light generation in free-electron lasers will be explained and important characteristics of FLASH are summarized. Some insight is given on optical layouts for guiding and focussing the XUV light.

In the second part of this chapter, the experimental setup for simultaneous scattering and ion spectroscopy of single clusters will be introduced. Crucial components of the experiments, such as the generation of clusters and the detection of scattered light and ions will be discussed in more detail.

2.1 FLASH Free-Electron Laser for Short Wavelength Radiation

Free-electron lasers (FELs) hold great promise as high power, short pulse, coherent sources for short wavelength radiation [1, 2]. The continuous progress in X-ray physics of the last century has been tightly coupled to the advancement of light sources. Since the discovery of x rays in 1895 by Wilhelm Conrad Röntgen [3] the brightness of X-ray sources has been increasing more than four orders of magnitude per decade in the last 50 years as shown in Fig. 2.1a [4]. This quantity, the brightness B , is defined as the number of photons n divided by the product of the beam area A , the opening solid angle of the radiation beam θ , the pulse length t and the fractional bandwidth of energy $\Delta E/E$,

$$B = \frac{n}{A \cdot \theta \cdot t \cdot \frac{\Delta E}{E}}. \quad (2.1)$$

The increase in brightness (or peak brilliance) is illustrated in Fig. 2.1b, where the capabilities of modern synchrotron sources and short wavelength free-electron lasers are displayed. The short and bright pulses of FLASH and LCLS exceed the other

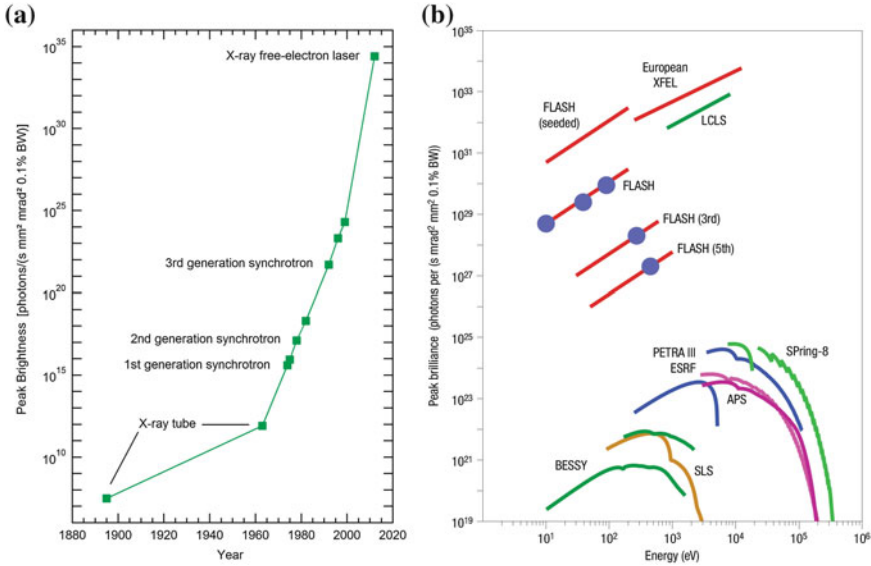


Fig. 2.1 **a** Development of peak brilliance of X-ray sources since 1895. Based on [4]. **b** Peak brilliance of modern X-ray light sources. From [5]

sources by more than seven orders of magnitude [5, 6]. A single FEL pulse of 10 to 100 fs duration typically contains 10^{12} – 10^{13} photons, as many as the best synchrotron radiation beamlines deliver in about one second [7]. In the following paragraph the underlying physical processes and technical principles are briefly reviewed. A more detailed compendium can be found in the literature [1, 2, 8].

2.1.1 Basic Principle of a Free-Electron Laser

Free-electron lasers and modern synchrotron sources share a common basic principle for the generation of light. Figure 2.2 illustrates the evolution of synchrotron sources from a simple bending magnet (Fig. 2.2a) to the use of magnet arrays (Fig. 2.2b–d) [9]. Electrons are accelerated to relativistic kinetic energies and forced on a slalom course through a periodic stack of alternated dipole magnets. With every turn, the electrons emit light. In a so called wiggler device, the amplitude of the electron trajectory is rather large and consequently also the solid angle in which the photons are emitted. This leads to an incoherent superposition of the radiation and the emitted power rises linear with the number of magnet pairs within the wiggler. In contrast, the emitted power in an undulator rises quadratically with the number of magnet pairs. The periodic deflection of the electrons is so small that the radiated light from an electron in every undulator period can overlap and thus interfere.

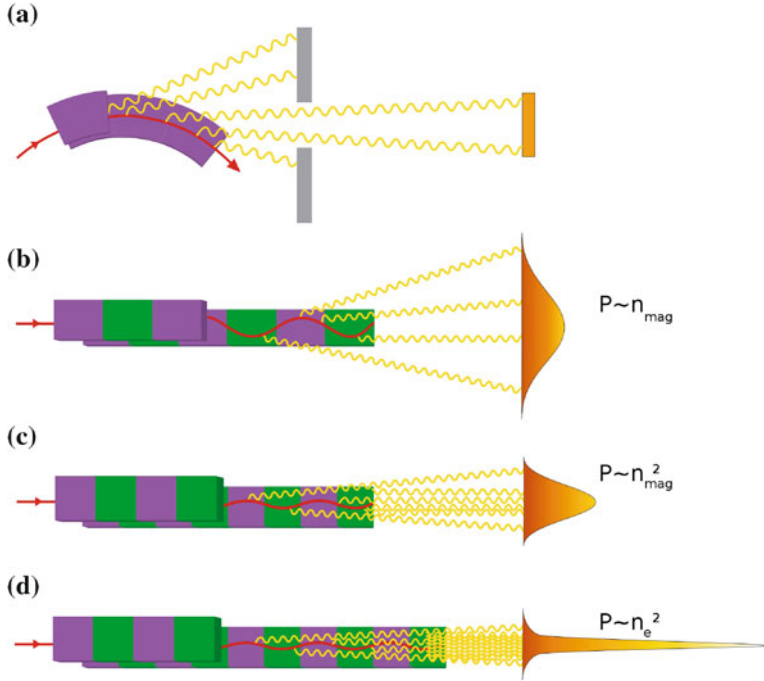


Fig. 2.2 Radiation of a bending magnet, a wiggler, an undulator and a free-electron lasers. P is the irradiated power in forward direction. Adapted from [9]. **a** Bending magnet. **b** Wiggler. **c** Undulator. **d** Free-electron laser

Constructive interference appears for a phase match between the electron energy and the undulator period, yielding a distinct resonant wavelength

$$\lambda_{res} = \frac{\lambda_u}{2\gamma^2} \left(1 + \frac{K^2}{2} + \gamma^2 \theta^2 \right), \quad (2.2)$$

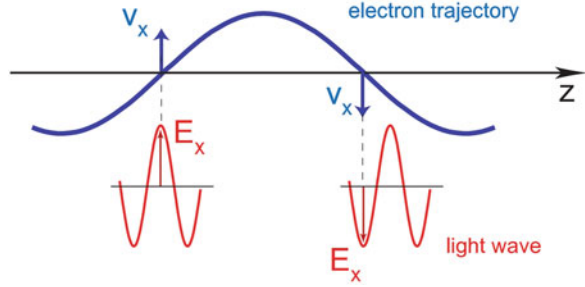
with the undulator period λ_u , the Lorentz factor $\gamma = (1 - v^2/c^2)^{-\frac{1}{2}}$, the undulator parameter K , and the observation angle θ . The dimensionless parameter K is a measure of the oscillation magnitude and is given by

$$K = \frac{eB\lambda_u}{2\pi m_e c}, \quad (2.3)$$

with the magnetic field B of the undulator. The K -parameter of a wiggler is > 10 , typical values for an undulator are in the order of 1.

The radiation of free-electron lasers is also generated in undulators but the emitted power does not only increase quadratically with the number of undulator periods but also with the number of electrons involved in the lasing process. The resonant

Fig. 2.3 Slippage of the light wave of one optical wavelength per undulator period. From [10]



wavelength of a free-electron laser is given by an equation equivalent to the undulator Eq. 2.2 with $\theta = 0^\circ$:

$$\lambda_{res, FEL} = \frac{\lambda_u}{2\gamma^2} \left(1 + \frac{K^2}{2}\right). \quad (2.4)$$

The electron energy matches the undulator period such that the light is overtaking the relativistic electrons by exactly one cycle while they move one undulator period further. This key process in free-electron laser physics displayed in Fig. 2.3 is referred to as *slippage*. The same phase relation is valid in an undulator for synchrotron radiation at $\theta = 0^\circ$ but there the interference effects apply independently to the radiation probability for each electron, with no inter-electron effects. The electrons can never experience their own light field as their velocity is always $< c$. However, in a free-electron laser the electrons are extremely well compressed into a small bunch with a very sharp kinetic energy distribution. These characteristics, the spatial and the velocity distribution of the electron bunch, are gathered in a quantity called *emittance*. A low emittance of the electron bunch is the basic condition for the lasing process. In this case a present electromagnetic field can interact back on the electrons and force them to stimulated emission.

The requirements on the quality of the electron bunch are therefore especially high for short wavelength FELs. As illustrated in Fig. 2.4a, in the infrared and visible regime it is possible to run free-electron lasers in the *low gain range*. In this concept a train of relativistic bunches recirculate within a storage ring through an undulator

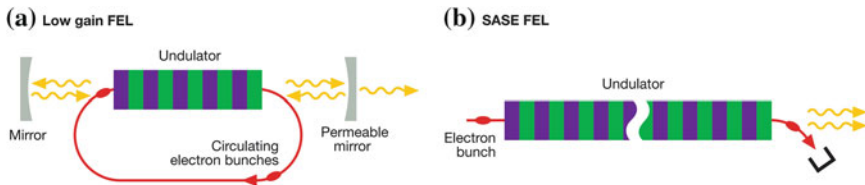


Fig. 2.4 **a** Principle of a low gain FEL working in the infrared or optical regime. **b** Principle of a high gain single-pass FEL. From [7]

placed in an optical cavity. A small gain in radiation power of a few percent per undulator passage is sufficient to allow output powers in the order of Gigawatts [7]. Even though the resonance wavelength of an undulator can be shifted into the X-ray range by just increasing the electron kinetic energy, no normal incidence optics with reflectivities $>90\%$ exist for wavelengths below 100 nm. Therefore, short wavelength FELs are built on the principle of a *single-pass high gain FEL* as displayed in Fig. 2.4b. Here, all radiation is generated in a single passage through a very long undulator. For accelerating the electrons linear accelerators are used as only they allow for preserving the low emittance of the electron bunches required for the lasing process.

As the electron bunch orbits through the undulator some of the electrons will be accelerated and take energy from the light field, others will be decelerated and contribute energy to the light field depending on their phase (cf. Fig. 2.3). Because of the slippage, the electrons experience the same light field in every phase of their oscillation, which makes the interaction very efficient. In the long undulator of a high gain FEL, the periodically modulated energy is then transformed into a density modulation, as the faster electrons catch up with the slower ones. This process will continue until the electrons in the bunch form a package of slices with a spacing of λ_{res} , so called *microbunches* (illustrated in Fig. 2.5). Microbunching will lead to an increase of the radiated power proportional to the number of microbunched electrons n_e squared because the electrons separated by λ_{res} radiate like a point charge $Q = n_e \cdot e$. The number of electrons contributing to the lasing process increases while the bunch passes the undulator, yielding an exponential growth of the emitted power with undulator length. In Fig. 2.5 the growth is shown as a function

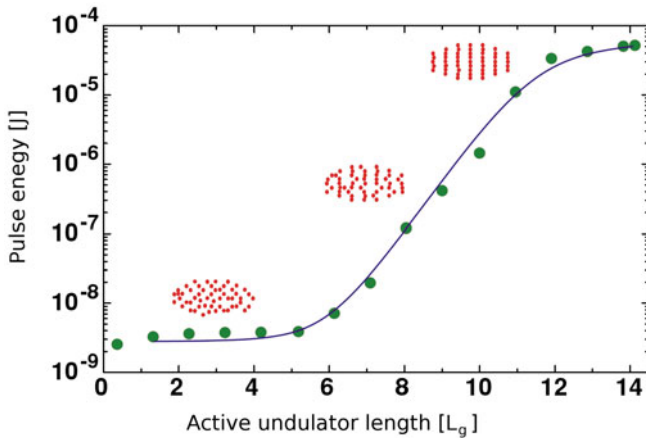


Fig. 2.5 Gain length and microbunching. In a single-pass FEL the density modulation of the electron bunch develops along the travel through the undulator. The gain curve shows exponentially growth of the output power until optimal microbunching is reached and the pulse energy saturates. Adapted from [1, 2]

of *gain length* L_g , the undulator length in which the power rises by a factor of e . After several L_g , when the microbunches are fully developed, laser saturation sets in.

In IR and visible FELs a concept is widely used which is referred to as *seeding*. In this case, the electromagnetic field which is amplified by the electrons is inserted from an external source such as a seeding laser. Another approach which is especially convenient for short wavelengths where less laser sources exist is spontaneous undulator radiation being used for amplification. This process is referred to as *SASE* (self amplified spontaneous emission). SASE is used in most of the current short wavelength FELs, for example at FLASH [5, 6]. Since the lasing starts from shot noise, the photon energy is subject to statistical fluctuations. SASE FEL radiation typically consists of more than one single pulse in time and frequency [11], even though SASE radiation also exhibits full transverse coherence [2]. As brighter pulses and smaller bandwidths can be achieved by seeding, concepts have also been developed for the short wavelength range. For example at FERMI, Trieste, a high-harmonic-generation (HHG) source is successfully used as seeding laser for an FEL in the VUV range [12]. At FLASH, there is also a seeding option under construction, using HHG [13]. Another approach for seeding short wavelength FELs is to monochromatize SASE radiation and use it as a seed beam in a second undulator [14, 15]. Such self-seeding has been recently demonstrated for hard x rays at LCLS using a diamond crystal to extract a narrow-banded part of a SASE pulse [16].

2.1.2 Characteristics of the FLASH FEL

FLASH, a linac based facility at DESY has been the first short wavelength free-electron laser in operation [18, 19]. Table 2.1 summarizes some important photon and pulse characteristics of FLASH. Typical parameters of the operation of FLASH from [17] are shown in the center column, the corresponding parameters used in the experiment for this work are displayed in the right column.

Table 2.1 FLASH pulse and photon characteristics

Parameter name	Typical values 2005–2009 [17]	Parameters of our experiment 2011
Wavelength range (fundamental)	6.5–47 nm	13.6 nm
Average single pulse energy	10–100 μ J	150 μ J
Pulse duration	10–70 fs	100 fs
Spectral bandwidth	1 %	1 %
Photons per pulse	10^{12}	10^{13}

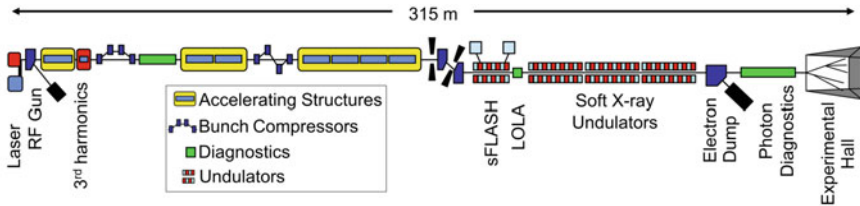


Fig. 2.6 Layout of the FLASH facility, see text for description. Adapted from [17]

In Fig. 2.6, the current layout of FLASH [7, 17] is displayed. The electrons are produced in the RF gun, a laser driven photocathode placed in a radio-frequency cavity. From the gun the electrons are accelerated to a maximal kinetic energy of 1 GeV in accelerator modules consisting of super-conducting niobium cavities. In between the accelerator modules the electron bunch is further compressed by inducing a chirp over the electrons and sending them through a bunch compressor, a small magnetic chicane. In addition Fig. 2.6 also contains the latest improvements and extensions such as an afterburner for enhancing the production of 3rd harmonic radiation and the sFLASH unit for HHG seeding.

The coherent radiation is produced in an undulator with a gain length of roughly 1 m and an overall length of 27 m. The undulator period of 24 mm with a 12 mm gap between the magnetic poles yields a magnetic field B of 0.5 T. Using Eq. 2.3 the K -parameter of the FLASH undulator is $K = 1.1$. Assuming a maximal electron energy of 1 GeV, Eq. 2.4 yields a minimal wavelength of 5 nm.

After the undulator, the electron bunch is extracted with a dipole magnet and sent into a beam dump. The light pulses emerge from the accelerator tunnel and enter the experimental hall. Several photon diagnostics are available at this stage, such as a spectrometer for wavelength determination and a gas monitor detector for online pulse energy measurements (for further details see [20]). The FLASH pulses can be guided into 5 different beamlines. Due to the strong absorption of soft X-ray radiation in any material, the beam is transported through a windowless UHV system. In the next paragraph brief insight is given in the possibilities of guiding and focussing the bright XUV light into the experiment.

2.1.3 Guiding and Focussing Optics for XUV Light

Due to the lack of lens materials, which could be used for short wavelength radiation from VUV to soft X-ray, other approaches become necessary. Mainly two types of mirrors are used to guide and focus XUV radiation [21].

Grating Incidence Mirrors are optics with a high transmission in an extended wavelength range. Plane carbon mirrors are for example used at FLASH to deflect the FEL beam into the different beamlines [22].

The basic principle of these mirrors corresponds to total internal reflection, widely used in the visible range for example in fiber optics. In the VUV to soft X-ray range, the real part of the refractive index of materials is typically slightly smaller than one ($n' < 1$). As total reflection always occurs from the optically thin medium, in the XUV *total external reflection* under gracing incidence can be used. The mechanism is sketched in Fig. 2.7a. Without any absorption, optimal reflectivity is yielded at the critical angle $\theta_{crit} = \sqrt{2\delta}$. However, an evanescent wave does penetrate the material up to a certain depth. Therefore, a finite absorption $\beta > 0$ results in an optimal reflectivity for incident angles smaller than θ_{crit} .

The surface material has to be selected according to the designated photon energy region. In the range relevant for FLASH, carbon coated mirrors are chosen due to their high reflectivity and flat absorption cross-section [23]. In Fig. 2.7b the reflectivity of a carbon mirror under 2° gracing incidence and the atomic photo absorption are displayed. The data is taken from the Henke tables [24].

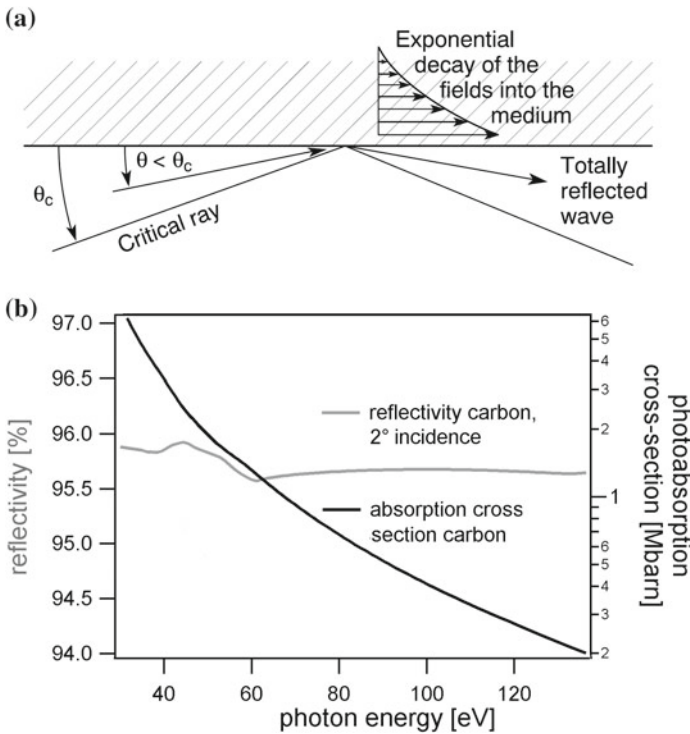


Fig. 2.7 a Principle of total external reflection of XUV radiation. From [21] b reflectivity of a carbon surface under 2° and photo absorption cross-section from 30 to 150 eV. Data from Henke tables [24]

Based on the principle of total external reflection, focussing optics can be manufactured as well. Carbon coated ellipsoidal mirrors with a focal distance of 2 m are installed at beamlines BL2 and BL3 producing a focus with 20–30 μm diameter (FWHM) [20].

Multilayer mirrors are the second approach for reflecting short wavelength light. Fig. 2.8a demonstrates that multilayer mirrors bridge the gap of (near-) normal incidence mirrors in the VUV to soft X-ray range [21].

The reflectivity at normal incidence of a material with refractive index $n = 1 - \delta + i\beta$ can be obtained by the Fresnel equations [25] to

$$R \simeq \frac{\delta^2 + \beta^2}{4} \ll 1. \quad (2.5)$$

Therefore, the normal incidence reflectivity on a surface will go down for higher wavelengths, where only small deviations of n from unity occur. However, a higher reflectivity can be achieved again by constructive interference of the reflection on many layers. In hard X-ray regime natural crystals can be used which exhibit atomic layer distances in the range of the wavelength. In XUV multilayer mirrors can be produced.

With sputtering techniques thin layers of two materials with different optical properties are deposited alternately on ultrasmooth substrates. The materials are chosen such that for both the absorption is low while they exhibit a great difference in the reflectivity, i.e., the real part of the refractive index. Incoming light propagates into the mirror through many layers. At every layer transition some light is reflected. For a distinct wavelength matching the modulation period, the reflected rays interfere constructively, producing an overall high reflectivity. For a photon energy of 91 eV or 13.6 nm wavelength respectively, highly reflecting MoSi multilayer mirrors with close to 70 % reflectivity can be manufactured [26] as shown by the curve for periodic design in Fig. 2.8b.

The reflectivity of multilayers is limited by the finite absorption of materials in the XUV and by the interface roughness between the layers. It is therefore lower than for grating incidence mirrors. Also only a rather narrow bandwidth is reflected. On the other hand, multilayer mirrors can be optimized to reflect either in (near-) normal incidence or for another arbitrary angle. This makes them favorable for many otherwise space consuming optical layouts. A number of experiments carried out in our group [27–30] were based on a back reflecting geometry using a multilayer mirror with a short focal distance. It could be mounted within an experimental setup and produced a smaller focal spot and thus higher power densities than a farer distant beamline optic. The procedure of optimizing and characterizing the focal density will be described in Sect. 2.2.4.

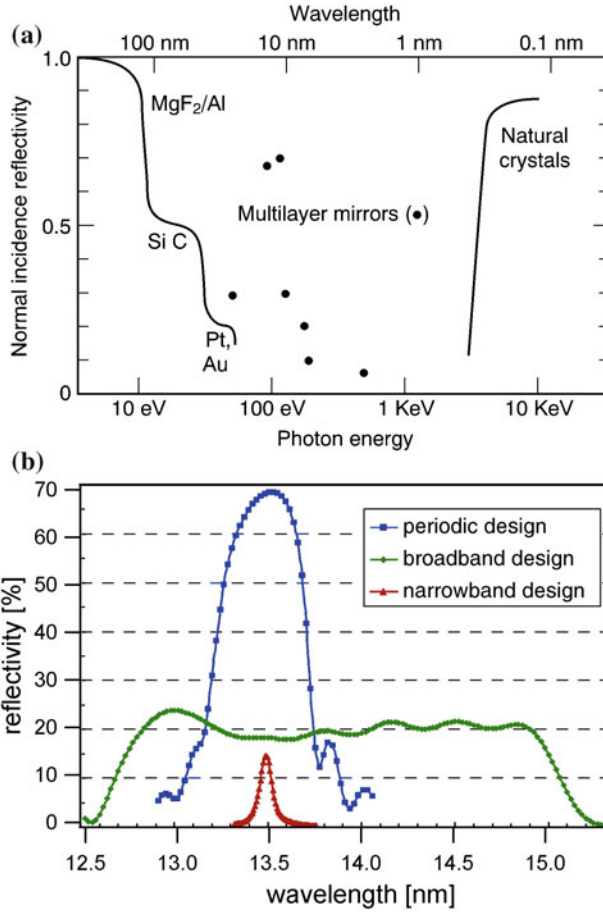


Fig. 2.8 **a** Possibility to produce near normal incidence mirrors from visible to X-ray regime. Multilayer mirrors close the gap in the XUV. From [21] **b** measured reflectivity of MoSi multilayer mirrors optimized for 13.5 nm. Adapted from [26]

2.2 Experiment for Imaging and Ion Spectroscopy of Single Clusters

In Sect. 2.1 the generation and handling of highly intense short pulses from the FLASH FEL have been introduced. This brilliant light source enables a new kind of experiments where individual particles can be studied in single pulses. In this section, the experimental setup developed for imaging and ion spectroscopy of single large clusters is described. Experimental principles and methods are laid out in more detail in the subsequent paragraphs.

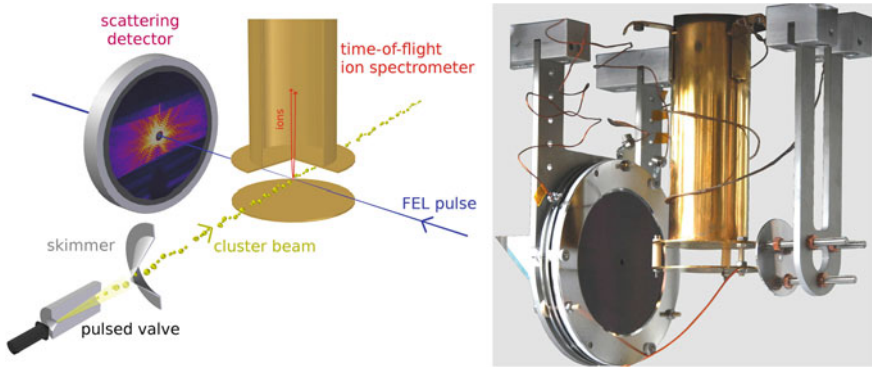


Fig. 2.9 *Left* setup scheme of the experiment for coincident imaging and ion spectroscopy of single clusters at FLASH. *Right* photo of the detectors assembled around the interaction region

2.2.1 Experimental Layout

The setup for simultaneous imaging and ion spectroscopy of single clusters at FLASH is displayed in Fig. 2.9. The experiment was carried out in July 2011 in the beamline focus of BL2, using 100 fs pulses with up to 10^{13} photons of 91 eV photon energy.

A cluster beam was generated by supersonic expansion of xenon gas through a cryogenically cooled, pulsed nozzle. The clusters were guided into the main chamber through a set of differentially pumped conical skimmers. Details on the cluster generation are discussed in Sect. 2.2.2. The cluster beam was further skimmed down by a movable piezoelectric driven skimmer slit with an adjustable width between 0 and 1.5 mm (cf. [31], not displayed in Fig. 2.9). Thus, the measurements could be done in “single cluster mode” at a target density with less than one cluster at a time in the focal volume.

The cluster pulse was spatially and temporally overlapping with the focussed FEL pulse. In a combined imaging and spectroscopy approach, two different kinds of products of the interaction were measured shot-to-shot, positively charged fragments of the clusters and elastically scattered light. The scattering patterns were detected by an MCP/phosphor screen stack as described in Sect. 2.2.3. The visible image on the phosphor screen was coupled out via a 45° mirror and recorded with an out-of-vacuum CCD camera. The FEL beam could exit the interaction region through a center hole in all components of the scattering detector. For the ion measurement the “bipolar tof” was used, as discussed in Sect. 2.2.4.

2.2.2 Cluster Generation

The rare gas clusters are produced in a supersonic gas expansion through a nozzle behind a pulsed valve. In this section a brief overview of the physics of supersonic jets is provided and the emergence of clusters in supersaturated gas is described. Also,

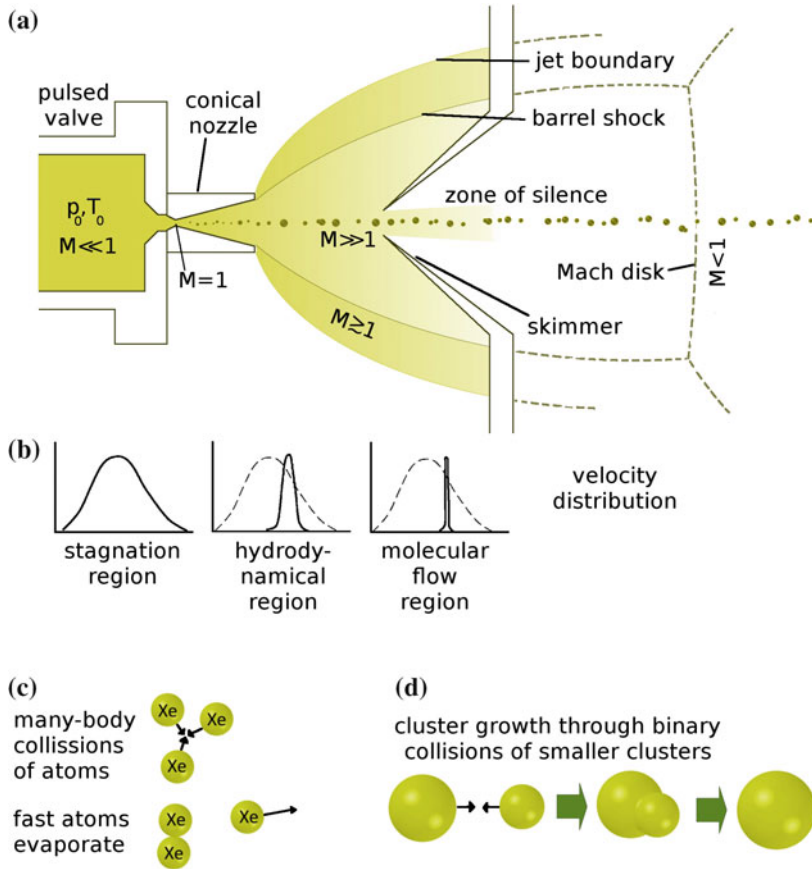


Fig. 2.10 **a** Schematics of a supersonic gas expansion through a conical nozzle. Shock waves surround the zone of silence in which clusters can grow. A skimmer guides the central part of the beam in a differentially pumped section before the Mach disk destroys the clusters. **b** Development of the particle velocity distribution in a supersonic gas expansion (adapted from [34]). **c** Mechanisms of cluster growth. At first, dimers are built through 3-body collisions. As long as the ratio of atoms to clusters is large, they grow through monomer addition. **d** Later, cluster-cluster aggregation becomes the dominant process

the mechanisms of cluster growth are explained and hence, scaling laws for cluster size distributions are presented. The temporal profile of cluster jets due to nozzle operation in pulsed mode is discussed. Finally, typical parameters of this experiment are summarized.

Conditions in a free jet: Free jets are widely used for the generation of cold atomic and molecular beams and also serve as a source for cluster beams [32, 33]. A free jet produced by supersonic expansion through a nozzle is schematically illustrated in Fig. 2.10a. Gas expands from a stagnation chamber with an initial pressure p_0 and a temperature T_0 through a small orifice with diameter d into vacuum. The expansion

exhibits three stages, the stagnation region, the hydrodynamic region and the molecular flow region [34]. The characteristic velocity distributions of these stages are displayed in Fig. 2.10b. In a supersonic expansion the random velocity of the atoms in the stagnation region is transformed into one-dimensional directed motion with a narrow relative velocity distribution. This is equivalent to a strong cooling of the gas. Equalization of the velocities takes place through collisions between the atoms. While the one dimensional flow velocity is rising, the particle density and thus the collision frequency decreases with the increasing distance to the nozzle throat. In particular, the number density of particles can be expected to decrease with the inverse square of distance, as the streamlines of the expanding gas resemble those of a point source flow [32]. At some point the jet leaves the collision dominated regime and enters the collision free molecular flow region, thereby reaching its terminal velocity. The maximum reachable flow velocity is given by

$$v_{\infty} = 1.581 \sqrt{\frac{2kT_0}{m}} = 204 \sqrt{\frac{T_0/K}{m/\text{amu}}} \frac{\text{m}}{\text{s}}, \quad (2.6)$$

with m being the atomic mass of the atoms.

Mach number: However, under realistic experimental conditions, the finite background pressure p_{back} in the expansion chamber limits the free expansion to a system of shock waves as sketched in Fig. 2.10a. The shock waves reflected by the background pressure at the sides of the expansion cone are referred to as *barrel shocks* and the region where the velocity changes from supersonic to subsonic within a short distance in axial direction is known as *Mach disk*. Within these boundaries of the expansion, in the *zone of silence*, the adiabatic expansion takes place. A measure for the development of the flow velocity is the Mach number M , the ratio of the gas flow velocity to the local sound speed. If $M > 1$ the particles move faster than information transport in the gas flow. Within the stagnation chamber M is much smaller than 1 while at the nozzle throat, M equals unity and then increases further in the hydrodynamic region with rising distance to the nozzle throat. In the boundary regions M drops again to below 1.

The position of the Mach disk from the nozzle throat is given by

$$\frac{x_{\text{Mach}}}{d} = 0.65 \sqrt{\frac{p_0}{p_{\text{back}}}}. \quad (2.7)$$

When reaching the Mach disk, the cold beam of atoms, molecules or clusters will be disturbed and reheated. Therefore, the Mach disk has to be located after the interaction region of the experiment. A practical possibility to shift the Mach disk away from the nozzle is to decrease p_{back} by using differential pumping stages (cf. Eq. 2.7). The central, i.e. coldest part of the flow is cut out and transported into a differentially pumped chamber with a lower background pressure through a skimmer with an optimized shape and diameter in order to not disturb the gas flow (cf. Fig. 2.10a).

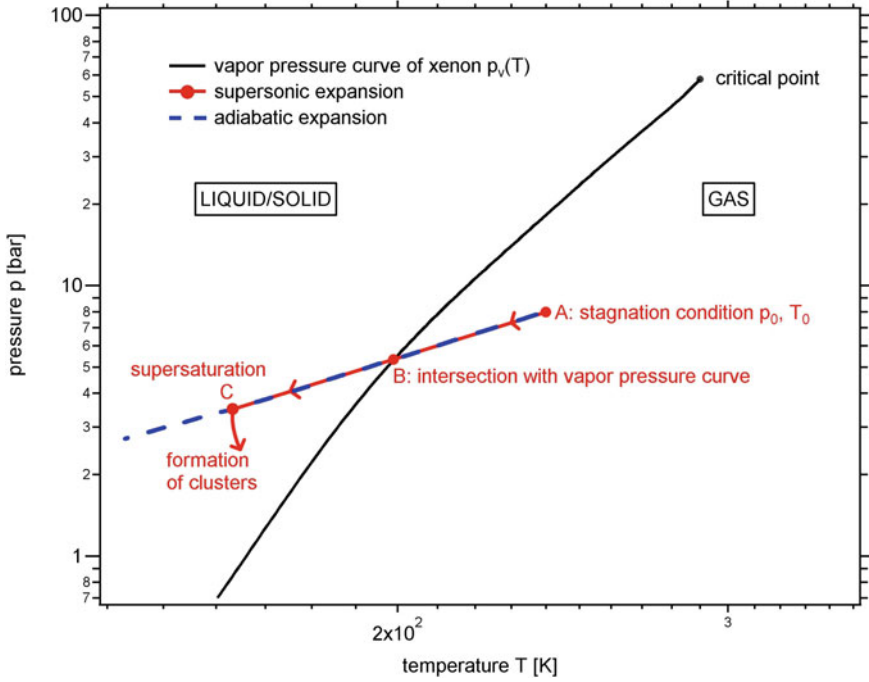


Fig. 2.11 Vapor pressure curve of xenon. The path of a supersonic expansion with cluster condensation is sketched in red. The data has been taken from [35], the expansion path is adapted from [32, 34]

Cluster formation: The formation of clusters in a free jet can be explained as a phase transition from gaseous into liquid or solid state. Whether clusters emerge in this expansion process or not depends on the final pressure and temperature of the flow and in particular, if those parameters have left the gaseous domain. Figure 2.11 illustrates the phase diagram of a supersonic expansion using the example of the vapor pressure curve of xenon (data from [35]). Typical stagnation conditions as used in this experiment ($p_0 = 8$ bar, $T_0 = 240$ K) are represented by point A. From there, the expanding gas follows the adiabatic line down to point B, where it meets the vapor pressure curve $p_v(T)$. Under equilibrium conditions the subsequent expansion would follow the vapor pressure curve. Instead, it proceeds along the adiabatic line into a regime of supersaturation. At point (C), condensation and formation of clusters sets in. At the same time the expansion departs from the adiabatic line and returns to the vapor pressure curve [32, 34].

As schematically illustrated in Fig. 2.10c the condensation process starts with the appearance of dimers formed in three-body collisions. Two atoms stick together, the third atom evaporates, taking away excess momentum and energy. When dimers are formed, they can act as condensation nuclei for further cluster growth. As long as the ratio of atoms to clusters in the jet is high the clusters grow through monomer

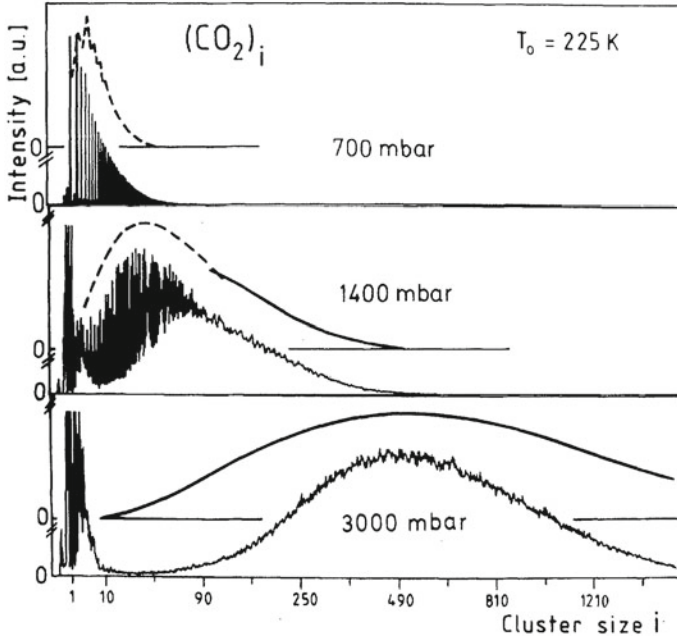


Fig. 2.12 Cluster size distributions for a supersonic expansion of CO_2 gas show the transition from monomer addition to cluster aggregation. The exponential decay at small cluster sizes is attributed to cluster growth through monomer addition, the lognormal size distribution developing for higher expansion pressures indicates coagulation of clusters. From [36]

addition. With rising numbers of clusters, *coagulation*, i.e. aggregation of smaller clusters will become the dominant process. Cluster growth through coagulation yields log-normal distributions of cluster sizes, whereas clusters generated from monomer addition form a size distribution with an exponential decay [36]. Typical cluster size distributions showing both of those features are displayed in Fig. 2.12.

Scaling laws for the average cluster size: The average final cluster size obtained with a distinct set of expansion parameters can be estimated using the empiric scaling laws developed by Hagena et al. [37]. For the same gas species, different combinations of the expansion parameters may lead to the same cluster size distribution. This relationship is expressed by the scaling parameter Γ as a measure for condensation [32],

$$\Gamma = n_0 d_{eq}^q T_0^{0.25q-1.5}. \quad (2.8)$$

The numerical value of the exponent q has been experimentally determined to be 0.85. n_0 denotes the number density, T_0 is the gas temperature. The *equivalent nozzle diameter* d_{eq} has to be used in case of a conical nozzle shape. For conical nozzles, the streamlines of the expansion are limited to the cone angle 2θ but remain otherwise unchanged. As the expansion cone of a simple orifice becomes less divergent for

increasing nozzle diameter, the streamlines of a conical nozzle with diameter d mimic those of a much larger orifice. Thus, conical nozzles can reach the same Γ -value at a much lower gas load than simple orifices. This is described by the equivalent nozzle diameter $d_{eq} = d \cdot 0.74(\tan \theta)^{-1}$.

In order to connect the scaling parameters for the condensation of different kinds of gases, similarity laws can be introduced. In short, all material specific properties of gas species are gathered in a factor K , for example $K = 5554$ in the case of xenon. A reduced scaling parameter Γ^* can then be expressed as

$$\Gamma^* = K \frac{p_0 d_{eq}^{0.85}}{T_0^{2.29}}, \quad (2.9)$$

with p_0 in mbar, d_{eq} in μm and T_0 in K.

Consequently, the average number of atoms in a cluster results as a function of Γ^* described by Hagena's scaling laws for different expansion regimes [38]:

$$\begin{aligned} \Gamma^* < 350 & \quad \text{no condensation} \\ 350 \leq \Gamma^* < 1800 & \quad \langle N \rangle = 38.4 \left(\frac{\Gamma^*}{1000} \right)^{1.64} \\ \Gamma^* \geq 1800 & \quad \langle N \rangle = 33 \left(\frac{\Gamma^*}{1000} \right)^{2.35}. \end{aligned} \quad (2.10)$$

For completeness it is mentioned, that for the regime of Γ^* between 10^5 and 10^6 a deviation from Hagena's law was proposed [39],

$$\langle N \rangle = 100 \left(\frac{\Gamma^*}{1000} \right)^{1.8}. \quad (2.11)$$

The cluster sizes in this experiment reach and exceed this regime. The obtained size distributions will be discussed in Sect. 3.3.

Cluster parameters of the experiment: Typical values of the parameter sets used in this experiment are summarized in Table 2.2. Such extreme expansion parameters are only possible in pulsed operation of the cluster beam because of the otherwise high gas load. FLASH light pulses as short as 100 fs are used at a repetition rate of 5 Hz. Thus, a great amount of pump load can be saved by opening the nozzle only 5 times per second using a pulsed valve. A solenoid driven valve (Parker 99 series [40]) as illustrated in Fig. 2.13a is mounted on a cryostat [41, 43].

To ensure stable expansion conditions, the opening time of the valve was typically set to 3 ms in our experiments. This is in good agreement with Rayleigh scattering measurements with the same valve type displayed in Fig. 2.13b [42]. There, a plateau was only found for valve opening times of 3 ms or longer. However, the cluster beam conditions changing with the timing of the light pulse in respect to the opening of the nozzle valve have been investigated in more detail in this work, as presented in Sect. 3.3.2. The analysis of the scattering measurements for different valve trigger delays revealed a sharper rise of the cluster pulse (cf. Fig. 3.11a) with a formation of a plateau within less than 1 ms.

Table 2.2 Typical parameters used for cluster generation

Parameter name	Typical values of our experiment
Nozzle d , θ , d_{eq}	200 μm , 4° , 2 mm
Gas	Xenon
p_0	8 bar
T_0	220 K
p_{back} in expansion chamber	$\approx 5 \times 10^{-3}$ mbar
p_{back} in diff. pump. stage	$\approx 5 \times 10^{-5}$ mbar
p_{back} in interaction chamber	$\approx 5 \times 10^{-7}$ mbar
First skimmer (upstream)	$\approx 50^\circ$ cone, 0.5 mm diameter
Second skimmer (downstream)	$\approx 50^\circ$ cone, 1 mm diameter
Valve opening time	3–8 ms

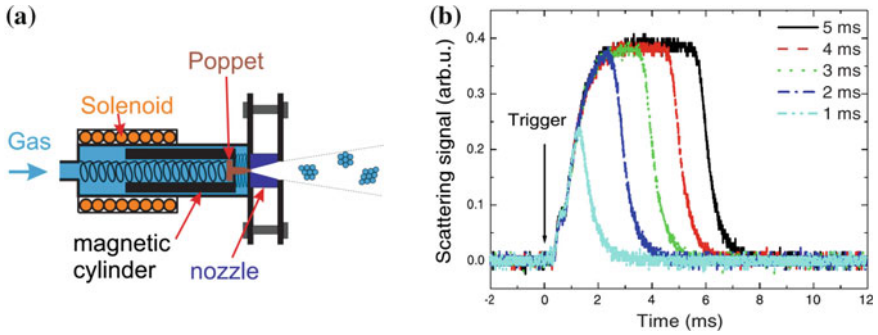


Fig. 2.13 **a** Function principle of the used solenoid valve (Parker 99 series [40]). Taken from [41]. Gas with a certain pressure and temperature fills the stagnation chamber. A magnetic cylinder with a sealing poppet is pressed by a spring into the nozzle throat. The solenoid pulls the cylinder with the poppet back, following a pulse trigger. Gas expands through the nozzle and may condense to clusters. **b** Time resolved Rayleigh scattering signal for different valve opening times [42]. The formation of a plateau was observed only for opening times longer than 2 ms

2.2.3 Detection of Scattered Light

The detection system for elastically scattered photons is the key component of the experiment. The position resolving area detector consists of a large-area multichannel plate (MCP) and a phosphor screen. Both have a 3 mm center hole for the exiting beam. A sketch of the detector is shown in Fig. 2.14a [44].

Multichannel plate: The working principle of a multichannel plate is sketched in Fig. 2.14b. An MCP can be understood as an array of miniature electron multipliers [45]. A plate with small, parallel channels is made from lead glass and coated with a material optimized for secondary electron emission (p.e. CsI). Between front and back of the plate, which are metal coated for electrical contact, a potential in the order

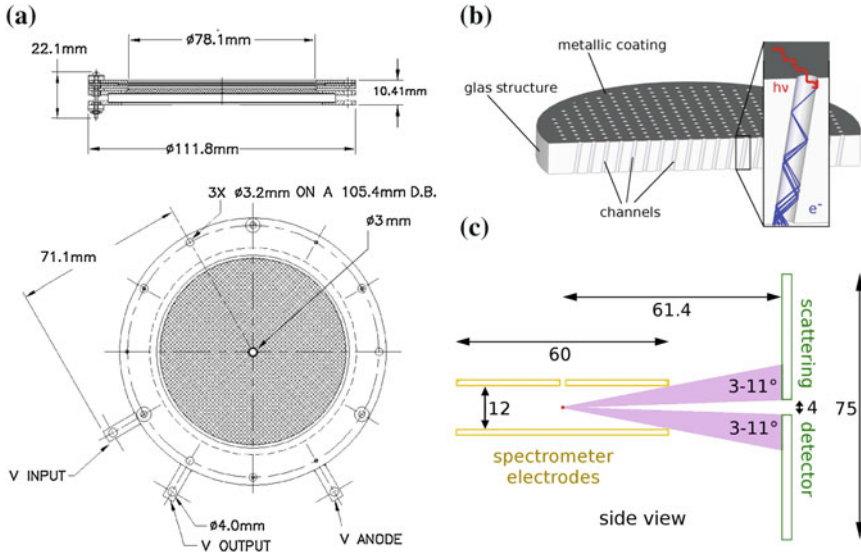


Fig. 2.14 Scattering detector **a** Large area MCP-phosphor stack with center hole. From [44] **b** function principle of a multichannel plate for photon detection. An incoming photon ejects electrons from the channel wall. The signal is amplified in a cascade of secondary ionization processes through the channel. **c** Side view of the detector geometry. The detection angle is limited to 11° by the shadow from the ion spectrometer electrodes. In vertical direction the diameter of the scattering detector of 75mm defines the maximal scattering angle of 31°

of 1000 V is applied. Incoming photons result in the emission of electrons from the channel walls which are multiplied along the channel. The channels of this specific detector have a diameter of $25\text{ }\mu\text{m}$ with a $32\text{ }\mu\text{m}$ spacing between two channels and a length to diameter ratio of 60 [44]. Their axis are tilted by an angle of 8° to the normal on the MCP input surface and two multichannel plates are stacked on each other in a so-called Chevron configuration [46]. This enhances the yield and minimizes the chance for secondary ions to drift from the back to the front and disturb the signal.

Phosphor screen: The electron avalanche exiting the back side of the back MCP is further accelerated towards a phosphor screen and transformed into an optical signal. P20-type phosphor is applied on a fiberoptic plate for obtaining high spatial resolution. It emits green light around 550nm wavelength with a decay time in the μs range. The visible image on the screen is then recorded by an out-of-vacuum CCD-camera. The linearity and efficiency flatness of this detector are discussed in the appendix to this thesis.

A hole in the center of the detector is necessary to guide the FEL beam out of the interaction region. It leads to an inactive area in the center of the detector with a diameter of about 4mm . Such an insensitive area is common to all kinds of small angle scattering experiments.

Detector geometry: The arrangement of detectors in the current setup has been displayed in Fig. 2.9. A sketch of the geometry with distances and angles is depicted in Fig. 2.14c. The scattering detector is placed 61.6 mm behind the interaction region. The electrodes of the time-of flight spectrometer with a diameter of 60 mm at 12 mm distance to each other cast a characteristic shadow on the scattering detector. With a diameter of 75 mm of the sensitive area and an inactive diameter of 4 mm, the scattering detector covers a scattering angle horizontally from about 3 to 31° , and vertically up to 11° . The scattering patterns visible on the phosphor screen are coupled out of the top flange by a 45° mirror with a center hole which is optimized to the oblong form of the patterns.

Reduction of ion signal and straylight: Besides elastically scattered photons, also high kinetic electrons and ions fly towards the scattering detector. They can add unwanted noise to the scattering signal or even completely bury it. Therefore the front of the MCP is biased with a high negative voltage, which slows down the electrons or pushes them away. In addition, by fast-switching the MCP voltage off early after the pulse, the photon measurement can be finished before the charged particles arrive. This method is referred to as *gating*. In this experiment, it was even possible to run the MCP in a constant mode and gate most part of the charged particles away by triggering the CCD camera adequately.

Already a single direct hit of the almost focussed FEL beam could seriously damage the scattering detector. While the adjustment operations as described in Sect. 2.2.4 were carried out, the MCP had to be covered with a solid screen plate. Final adjustment steps were taken without the screen using a gradually less attenuated beam. A well adjusted set of straylight apertures defined and guided the beam during operation, also protecting the system in case of slight movements of the FEL beam.

2.2.4 Ion Detection

In the first paragraph of this section the basic experimental principles of ion time-of-flight spectroscopy are described. The second paragraph will then summarize characteristics of the spectrometer used in this experiment. In the third paragraph, the procedure for optimizing the overlap of the laser and the cluster beam at highest power density using the time of flight spectrometer is discussed.

Time-of-flight spectrometer: For ion detection a time-of-flight (tof) mass spectrometer was implemented in the setup, which is displayed in Fig. 2.9. A system of electrodes accelerates and guides the ions produced in the interaction region towards a time resolving detector. The mass-over-charge ratio of the ions and their initial kinetic energy are determined by their flight time.

A tof spectrometer with a single acceleration stage is used in our setup, as depicted in Fig. 2.15a. The created ions are accelerated over a distance d_1 by a voltage U_{acc} applied between two plates. The ions reach a velocity v_1 which depends in first approximation only on their mass and charge. Through an aperture or a mesh, they

enter the field-free drift region of length d_2 , where their different velocities lead to an increasing difference in time of flight and thus to a better resolution. By solving the equation of motion in the acceleration region for t_1 , the moment when the ions enter the drift tube, one obtains

$$t_1 = \sqrt{\frac{4d_1^2}{U_{acc}} \cdot \frac{m}{q}}.$$

v_1 can be calculated to

$$v_1 = a \cdot t_1 = \sqrt{U_{acc} \cdot \frac{q}{m}}.$$

The time t_2 the ions need to pass the drift region with constant velocity is

$$t_2 = \frac{d_2}{v_1} = \sqrt{\frac{d_2^2}{U_{acc}} \cdot \frac{m}{q}}.$$

As a result, the overall time of flight can be calculated to

$$tof = t_1 + t_2 = \sqrt{\frac{m}{q}} \cdot \frac{2d_1 + d_2}{\sqrt{U_{acc}}} = const \cdot \sqrt{\frac{m}{q}}. \quad (2.12)$$

Bipolar TOF: Figure 2.15a displays a scheme of the “bipolar tof” spectrometer, which has been used in this setup. A sketch of the detector mounted on a CF63 flange is displayed in Fig. 2.15b and an image of its components is shown in Fig. 2.15c.

Ions created in the interaction region are accelerated by a voltage of 500 V over a distance $d_1 = 6$ mm before they enter the grounded drift tube through an aperture with 1.7 mm in diameter. The aperture opening is comparable to the Rayleigh length of the FEL focus in the order of 1 mm, restricting the interaction volume to the region of highest power density.

After a drift distance $d_2 = 142$ mm the ions pass a mesh and are then post-accelerated over a very small distance towards an MCP to enhance detection efficiency. The energy of the ion impact on the MCP plate is transformed into an avalanche of electrons, as explained in the last section, cf. Fig. 2.14b. For ion measurements the MCP detection probability and the signal intensity in general depend upon the atomic mass, the charge and impact kinetic energy of the ions [47]. For xenon ions with kinetic energies of at least 3.1 keV (cf. voltages in Fig. 2.15a), the detection probability is one, as every ion reaching the MCP ejects several electrons [47]. However, the output signal of the MCP will depend on the number of electrons ejected until at a certain point saturation is reached. Fig. 2.16 displays efficiency curves as a function of ion mass for different impact energies, calculated and measured for carbon based molecules. The curves for xenon might differ, but a first-order estimation can be done based on this graph. The ion with lowest efficiency in the current experiment, Xe^{1+} is indicated in blue. For an acceleration of $(0.5 + 2.6)$ keV

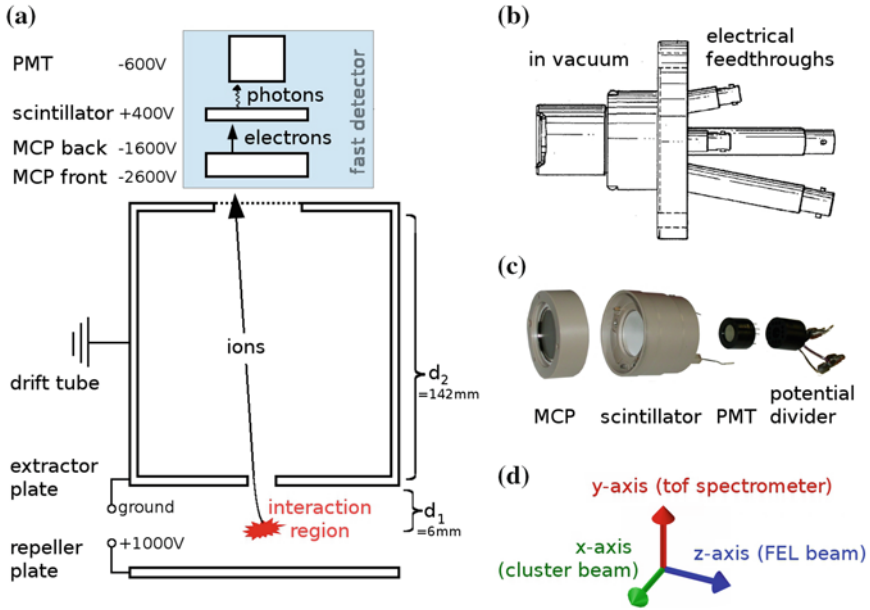


Fig. 2.15 *Bipolar tof* **a** scheme of ion tof spectrometer with bipolar detector and operation voltages. **b** Draft of the bipolar detector mounted on a CF63 flange. **c** Components of the bipolar detector assembly. **d** Coordinate system of the experiment (see text)

the MCP is already operating close to saturation and the signal from ions with finite initial kinetic energy and higher charge states will be amplified even more. Therefore, to simplify the discussion in Sect. 3.4 the MCP detection efficiency will be assumed to be in saturation.

The electron pulse is subsequently accelerated towards the scintillator. A fast photodiode detects the sparks on the scintillator. This signal is coupled out by a potential divider, digitized and stored on a PC. Therefore the digital transient recorder *Acquiris* [48] is used, providing high-speed signal measurement with a temporal resolution of up to 250 ps and 8 gigasamples per second.

Possible limitations of the mass resolution of a time of flight spectrometer consist in the resolution of the fast ion detector itself, the size of the interaction region and the initial kinetic energies of the ions. By choosing suitable electrode geometries and voltages or by using more than one acceleration stage, the resolution can be optimized to time-focus ions with the same $\frac{m}{q}$ but different points of birth or initial kinetic energy, respectively. This is for example realized for experiments with an extended interaction region in the so called Wiley–McLaren configuration [49].

In contrast, the specific spectrometer used in this experiment was designed in a non-Wiley–McLaren configuration. Thereby, initial kinetic energy distributions of the cluster ions can be resolved (cf. Sect. 3.4).

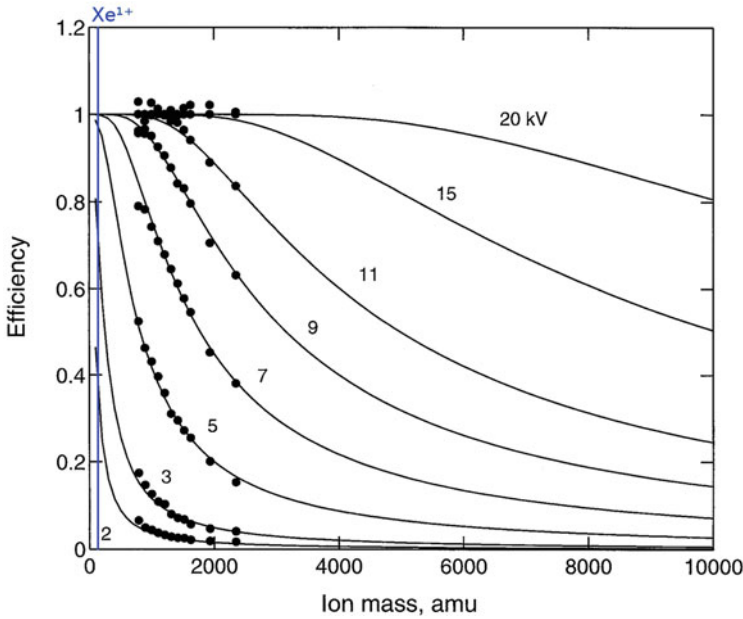


Fig. 2.16 MCP efficiency curves as a function of ion mass for different impact energies on the MCP [47]. The *lines* are calculated efficiency curves, the points are measurements for carbon clusters. In principle the curves might differ for different atomic species. For a simplified estimation, singly charged xenon is indicated in *blue*. Without initial kinetic energy, the Xe^{1+} will impact with 3 kV energy, i.e. at 70 % efficiency. The signal from higher kinetic energies and charge states will be amplified more

At the smallest focal waist already a very sharp spatial distribution is obtained. However, the broadening of the ion signal for positions far away from the smallest focus diameter can be observed in Fig. 2.17b in the smeared-out structure of the Xe^{2+} signal far away from the focal waist (green spectrum).

From Fig. 2.17, a mass resolution $\frac{\Delta m}{m}$ of 285 can be calculated from the width of $^{132}\text{Xe}^{2+}$ of 0.23 u. Thus, with the bipolar tof, in the focus of the FEL beam the isotope structure of xenon can be fully resolved.

Focus optimization and characterization: The interaction region is defined by the overlap between cluster beam and FEL focus. This requires a couple of optimization procedures for which the ion spectrometer is used. At the end of the optimization process, a characterization of the focal power density is carried out using the tof spectrometer.

In this paragraph, optimization and characterization procedures are explained by using a left-handed coordinate system as displayed in Fig. 2.15d: \vec{x} is set on the axis of cluster beam, \vec{y} lies on the axis of tof-spectrometer, and \vec{z} is equivalent to the FEL axis. The interaction region has to be adjusted to the position of the tof aperture and

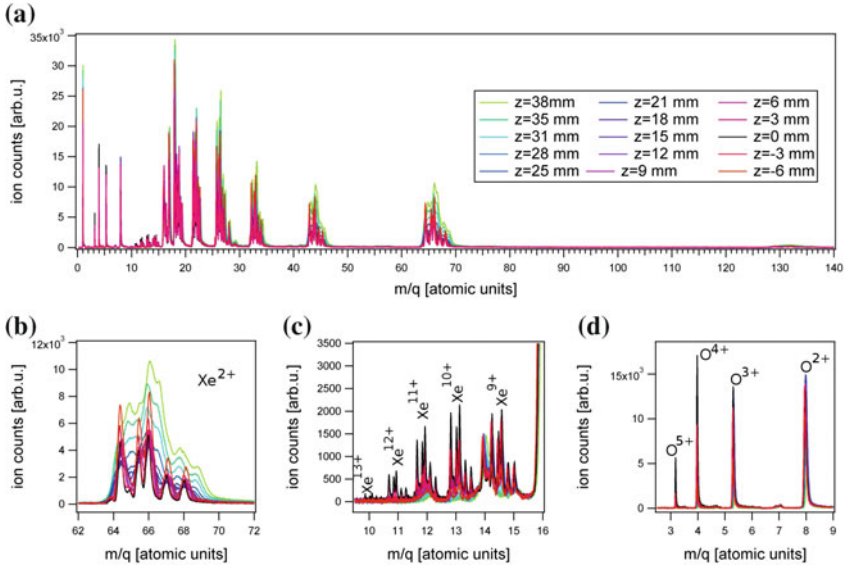


Fig. 2.17 **a** Time-of-flight spectra of xenon and residual gas atoms for different z -positions of the chamber along the FEL axis. **b** Xenon $2+$. For positions far away from the smallest focal waist, the increased focal volume results in a poor resolution. **c** Position of highest power densities is defined as $z = 0$ mm. Here, xenon charge states up to $13+$ are observed. **d** Higher charge states of oxygen from the residual gas up to O^{5+} also indicate highest power density for the *black curve*

the cluster beam alignment. The alignment procedure for the FEL beam is therefore carried out in three steps:

1. Optimize the position of the FEL beam relative to the tof aperture in \vec{x} direction. Ions from background gas, such as water become apparent in the ion spectrum when the FEL beam is located below the tof aperture.
2. Adjust the height of the FEL beam to overlap with the cluster beam. The optimal position is found by optimizing on cluster specific signal as singly charged xenon ions.
3. Optimize the focal power density by shifting the FEL focus in respect to the spectrometer along the \vec{z} axis. Optimization is done by scanning for nonlinear charge states, for example of xenon gas, i.e. charge states $> Xe^{6+}$ which can not be reached with single photon processes [50].

All three steps require a relative movement of the beam to the interaction region. This experiment was carried out in the beamline focus of BL2 at FLASH, which can not be easily moved. It is more practicable to move the experimental chamber around the FEL beam. Therefore the chamber is equipped with motorized bearings. However, in experiments using a back-focussing multilayer mirror as [28, 29], the mirror was tilted or moved along the beam axis.

The results of the focus scan for optimizing the setup in advance to the measurements for this work are displayed in Fig. 2.17. The spectra of atomic xenon for different z -positions reveal the position of the black curve to be at highest focal power density. Higher charge states of oxygen from the residual gas up to O^{5+} also indicate highest power density at this position, which is therefore defined as $z = 0$. A maximum charge state of $13+$ for xenon was detected which indicates a focal power density of $\sim 5 \times 10^{14} \frac{\text{W}}{\text{cm}^2}$ [50]. With a pulse energy of $150 \mu\text{J}$, a focus diameter of $20 \mu\text{m}$ can be calculated. However, it is important to note, that the actual pulse duration in the experiment of 100 fs was about a factor of 5 longer than in the cited reference. This can lead to equally high charge states at lower power densities as the photon flux is higher.

References

1. Z. Huang, K.J. Kim, Review of x-ray free-electron laser theory. *Phys. Rev. Spec. Top.* **10**, 034801 (2007)
2. J. Feldhaus, J. Arthur, J. Hastings, X-ray free-electron lasers. *J. Phys. B* **38**, 799–819 (2005)
3. W.C. Röntgen, On a new kind of rays. *Nature* **420**(53), 274–276 (1896)
4. S. Hau-Riege, *High-Intensity X-Rays*, Interaction with Matter (Wiley, New York, 2011)
5. W. Ackermann et al., Operation of a free-electron laser from the extreme ultraviolet to the water window. *Nature Photon.* **1**(6), 336–342 (2007)
6. P. Emma et al., First lasing and operation of an ångstrom-wavelength free-electron laser. *Nature Photon.* **4**(9), 641–647 (2010)
7. J. Schneider et al., *FLASH. The Free-Electron Laser in Hamburg*, Deutsches Elektronen Synchrotron DESY (2007)
8. J. Falta, T. Möller, *Forschung Mit Synchrotronstrahlung* (Vieweg und Teubner, Braunschweig, 2010)
9. I. Flegel et al. *BlitzLicht*. Deutsches Elektronen Synchrotron DESY (2007)
10. P. Schmüser, Fel theory for pedestrians. *Lecture at Heraeus seminar Free-electron lasers: From fundamentals to applications* 2012
11. R. Mitzner et al., Spatio-temporal coherence of free-electron laser pulses in the soft x-ray. *Opt. Express* **16**(24), 19909–19919 (2008)
12. E. Allaria et al., The FERMI@Elettra free-electron laser source for coherent x-ray physics: photon properties, beam transport system and applications. *New J. Phys.* **12**, 075002 (2010)
13. J. Bödeadt. sFLASH—first results of direct seeding at FLASH, in *Proceedings of FEL* (Malmö, Sweden, 2010)
14. J. Feldhaus et al., Possible application of X-ray optical elements for reducing the spectral bandwidth of an X-ray SASE FEL. *Opt. Commun.* **140**, 341–352 (1997)
15. E. Saldin et al., X-ray FEL with a meV bandwidth. *Nucl. Instrum. Methods Phys. Res. A* **475**, 357–362 (2001)
16. J. Amann et al., Demonstration of self-seeding in a hard-X-ray free-electron laser. *Nature Photon.* **180** (2012)
17. <http://flash.desy.de> DESY homepage
18. J. Rossbach, Short-wavelength single-pass free-electron lasers, in *Proceedings of LINAC2002* (2002)
19. J.R. Schneider, FLASH - from accelerator test facility to the first single-pass soft x-ray free-electron laser. *J. Phys. B* **43**, 194001 (2010)
20. K. Tiedtke et al., The soft x-ray free-electron laser FLASH at DESY: beamlines, diagnostics and endstations. *New J. Phys.* **11**, 023029 (2009)

21. D. Attwood, *Soft X-Ray and Extreme Ultraviolet Radiation* (Cambridge University Press, Cambridge, 2007)
22. J. Feldhaus, FLASH—the first soft x-ray free-electron laser user facility. *J. Phys. B* **43**, 194002 (2010)
23. B. Steeg et al., Total reflection amorphous carbon mirrors for vacuum ultraviolet free-electron lasers. *Appl. Phys. Lett.* **84**(5), 657–659 (2004)
24. Online data base for X-ray optical constants. http://henke.lbl.gov/optical_constants/
25. E. Hecht, *Optik*, 4th edn. (Oldenbourg Verlag, Berlin, 2005)
26. T. Feigl et al., EUV multilayer optics. *Microelectron. Eng.* **83**, 703–706 (2006)
27. C. Bostedt et al., Ultrafast x-ray scattering of xenon nanoparticles: imaging transient states of matter. *Phys. Rev. Lett.* **108**, 093401 (2012)
28. D. Rupp et al., Identification of twinned gas phase clusters by single shot scattering with intense soft x-ray pulses. *New J. Phys.* **14**, 055016 (2012)
29. M. Krikunova et al., Ionization dynamics in expanding clusters studied by XUV-pump-probe spectroscopy. *J. Phys. B* **45**, 105101 (2012)
30. M. Mueller et al, Fluorescence of xenon clusters as a probe for strong absorption XUV FEL pulses (in preparation, 2013)
31. M. Sauppe, Untersuchung der Ionisationsdynamik von Xenonclustern mit zeitaufgelöster Massenspektroskopie und mit Streumethoden, Master Thesis, TU Berlin, 2013
32. O.F. Hagena, Cluster ion sources. *Rev. Sci. Instrum.* **63**(4), 2374–2379 (1992)
33. G. Scoles, *Atomic and Molecular Beam Methods 1* (Oxford University Press, Oxford, 1988)
34. I. Yamada et al., Materials processing by gas cluster ion beams. *Mater. Sci. Eng.* **34**, 231–295 (2001)
35. Air Liquide online data base. <http://encyclopedia.airliquide.com/encyclopedia.asp>
36. J.M. Soler et al., Microcluster growth: transition from successive monomer addition to coagulation. *Phys. Rev. Lett.* **49**(25), 1856–1860 (1982)
37. O.F. Hagena, Nucleation and growth of clusters in expanding nozzle flows. *Surf. Sci.* **106**, 101–116 (1981)
38. U. Buck, R. Krohne, Cluster size determination from diffractive He atom scattering. *J. Chem. Phys.* **105**(13), 5408 (1996)
39. F. Dorchies et al., Spatial distribution of cluster size and density in supersonic jets as targets for intense laser pulses. *Phys. Rev. A* **68**, 023201 (2003)
40. Files/Precision Fluidics Division/UpdatedFiles/PulseValves.pdf. Data sheet Parker—General Valve, pulsed solenoid UHV valve 99 series. <http://www.parker.com/Literature/Literature>
41. S. Schorb, Size-dependent ultrafast ionization dynamics of nanoscale samples in intense femto-second x-ray free-electron laser pulses, Ph.D. Thesis, TU Berlin, 2012
42. G. Chen et al., Pressure dependence of argon cluster size for different nozzle geometries. *J. Appl. Phys.* **106**, 053507 (2009)
43. H. Thomas, Wechselwirkung von Edelgas-Clustern mit intensiven Pulsen weicher Röntgenstrahlung vom Freie-Elektronen-Laser FLASH, Ph.D. Thesis, TU Berlin 2009
44. Photonis. Quote and technical specifications of apd 3075 ps 32/28/8 i edr60:1 csi 3.0ch p20, 2011
45. J.L. Wiza et al., Microchannel plate detectors. *Nucl. Instrum. Methods* **162**, 587–601 (1979)
46. W.B. Colson et al., High-gain imaging electron multiplier. *Rev. Sci. Instrum.* **44**(12), 1694–1696 (1973)
47. I.S. Gilmore, M.P. Seah, Ion detection efficiency in SIMS: dependencies on energy, mass and composition for microchannel plates used in mass spectrometry. *Int. J. Mass Spectrom.* **202**, 217–229 (2000)
48. Acquiris data sheet. <http://www.home.agilent.com/en/pd-1197891-pn-U1056B>
49. W.C. Wiley, I.H. McLaren, Time-of-flight mass spectrometer with improved resolution. *Rev. Sci. Instrum.* **12**(26), 1150 (1955)
50. A.A. Sorokin et al., Photoelectric effect at ultrahigh intensities. *Phys. Rev. Lett.* **99**(21), 213002 (2007)

Ionization and Plasma Dynamics of Single Large Xenon
Clusters in Superintense XUV Pulses

Rupp, D.

2016, XIV, 161 p. 85 illus., 45 illus. in color., Hardcover

ISBN: 978-3-319-28647-1